Differential Least-Square Microwave Thermometry: A Feasibility Study on a Realistic Patient Model

Morteza Ghaderi Aram[†]*

(e-mail: morteza_ghaderi@ee.kntu.ac.ir).

Abstract

Microwave thermometry (MWT), among all the non-invasive thermometry methods proposed so far, stands a good chance to close the feedback loop of Hyperthermia (HT) systems in a cost-effective fashion. Previous studies in this context proved the suitability of the method when applied to simple scenarios. There remain, however, a lot of challenges to be addressed before the method can pave its way toward a successful clinical integration into the Hyperthermic systems currently in use. Dealing with a realistic patient scenario, the present study tries to cast light on some of the challenges/ pitfalls of MWT implementation. To this end, Comsol was used as the full-wave EM simulation package of choice, while its thermal result was cross-checked with that of a customized open-source computational platform, called FEniCS. Assuming that the dielectric properties of tissues change slightly under Hyperthermic thermal stress, the well-established differential linear least-square inversion method was then used to obtain a thermogram of property changes in the steady-state phase of the treatment. By successfully retrieving the tangible property changes at the HT focal point and by also capturing some of the hotspot locations, the inversion method sounds promising for being utilized in realistic scenarios. Nevertheless, the final image is still cluttered with reconstruction artifacts, demanding the application of a more rigorous inversion/ image restoration technique in future studies.

Index Terms

Microwave Imaging (MWI), MW Thermometry, Inverse Scattering, Bio-electromagnetics.

I. Introduction

Built upon the notion of inverse electromagnetic scattering [1, 2], microwave imaging [3]–[5] has been widely used for different applications ranging from non-destructive testing [6] to GPR prospecting [7, 8]. It has also found widespread medical applications, such as breast cancer detection [9], that form the diagnostic branch of the inter-disciplinary field of research, better known as Bio-Electromagnetics (BioEM). By targeting focused EM energy at the tumors under treatment, hyperthermia (HT) for the therapeutic BioEM [10, 11] has shown promising results to improve the outcomes of routine cancer treatment modalities such as radiotherapy and chemotherapy. The fusion of these two branches during recent years has resulted in a theranostic methodology, known as microwave thermometry (MWT) [12]–[15], which is the subject of further study in this article.

During the course of active research over the past decade or so, the EM packages and multi-physics simulation tools have increasingly become an indispensable part of the hyperthermia treatment planning (HTP) [16]. They have proved to be extremely helpful in the pre-treatment clinical phase because they not only assist clinicians to foresee

[†]M. G. Aram was formerly a student at Chalmers University of Technology where this research was partly conducted.

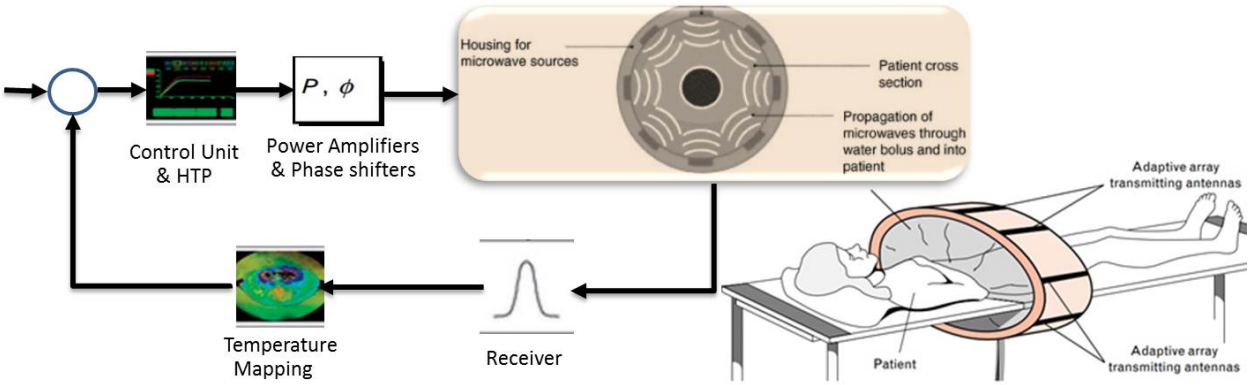

Fig. 1. The block diagram of a typical microwave HT system with the emphasis on the need for a monitoring feedback loop.

the potential rise of hot spots in a patient-specific manner, but they can also provide the necessary optimization tools to steer the focal point on tumors and to spare the healthy tissues from excessive heating. Whereas the optimized setting coming from a good treatment planning guarantees a safe and reasonable starting point for the treatment, it falls short of maintaining the same quality metric throughout the whole treatment session of nearly one hour. This is because the situation is dynamic and bound to change due to tissue property changes under thermal stress, not to even mention slight changes in the target position through inevitable patient movements along the long course of HT treatment. As shown in Figure 1, this necessitates an active monitoring mechanism that can track the thermal evolution in the region of interest, provide closed-loop feedback, and finally adjust the phased-array setting to avoid any drift in the focal point and hence maintain a high-quality metric throughout the treatment session.

As proposed in the ever-growing literature, the feedback loop can be realized through various means and methods ranging from invasive fiber-optic probes to MR-thermometry. Currently, the invasive method based on fiber optic catheters [17] and the minimally-invasive endoluminal thermometry [18] are the most common types of temperature measurements in clinical HT trials. Both methods are painful and may cause late complications. Moreover, the invasive thermometry provides only limited information about the volumetric temperature distributions due to restrictions on the placement of the catheters/ thermal probes. Therefore, to improve the treatment outcomes and patient's comfort, the growing trend in the field has been towards non-invasive techniques such as magnetic resonance (MR) [19, 20], ultrasound [21], and microwave thermometry (MWT).

MR-thermometry has been clinically proven as a reliable real-time temperature monitoring technique. It has a high spatial resolution and anatomical coverage per unit time [19], but it is not suitable for intraoperative monitoring in patients with MR incompatible pacemakers or artificial heart valves. It is also expensive and thus not affordable for all clinical centers. In this context, MWT ,in particular, stands out because, upon successful implementation, it will utilize the same microwave heating system for thermal monitoring as well which can obviously provide a very cost-effective and compact solution.

Previous studies [12, 14, 15] have investigated the possibility of utilizing microwave imaging techniques for the purpose of heat monitoring. They proved the suitability of the techniques and gave promising results. However,

they were all conducted mainly on simple scenarios, e.g. on cylindrical/spherical target regions embedded in a homogeneous medium. When dealing with realistic scenarios of microwave HT or ablation, on the other hand, there are many challenges arising from the intricate, inhomogeneous nature of the human tissues that need to be considered and addressed carefully. To this end, the present study, dealing with a realistic patient model that has a big tumor in the tongue region, tries to shed some light on the challenges and/or pitfalls lying ahead in the implementation of the MWT techniques proposed before.

II. Materials and Methods

There are plenty of commercial multi-physics software simulation packages that can be used in the workflow of HTP [16] and subsequent thermometry simulations such as CST Studio Suite®, ANSYS HFSS, Sim4Life, and COMSOL Multiphysics®, to name but a handful. That the different active research groups in the field choose one package in the HTP phase over another seems to be mostly a matter of convenience and previous exposure and/or familiarity of a group to the underlying numerical techniques used as the core computational engine of these simulators. Nevertheless, there have not been significant differences in HTP results and quality metrics reported in the open literature as a result of choosing one specific package over another. For instance, CST Microwave Studio in the studies conducted recently by Aram et. al. [22, 23] was the package of choice that yielded satisfactory results. This choice, however as explained below, turned out to have an enormous impact in the course of this study when it came to implementing the thermometry phase.

According to [24, 25], the key concept of the integrated numerical characterization, upon which the differential microwave thermometry technique was based, is to use the simulated E-field distribution of the baseline scenario as the Born approximation of the total internal field in the imaging kernel. Here the differences between the underlying method of FDTD in CST used for voxel models and that of FEM in Comsol used for CAD models come to play a significant role. While the triangulation of FEM meshes can be considered as a first-order field interpolation of the adjacent subdomains, the rectangular partitioning of the FDTD method is a zero-order field interpolation of the cubic subdomains that are prone to give rise to the stair-case approximation and sharp field variations at the tissue borders. When used in the kernel of an imaging method, these numerical artifacts in the E-field distribution can simply drown out the small variations due to heat which are the desirable information to be detected. In mathematical terms, these spurious numerical artifacts can render the whole imaging scheme ineffective by adding to the ill-posedness of the inverse problem at hand, resulting in a matrix with a very big condition number. Therefore, this was the reason why the authors chose Comsol over CST for this study, despite all the difficulties and limitations that the current version of Comsol has when it comes to importing and handling a big, intricate realistic human model as will be discussed in detail in the forthcoming subsection.

A. Patient model and the Hyperthermic applicator

The voxel model of a healthy 34-year-old man called Duke [26] was modified by inserting a relatively large tongue tumor in it, as shown in Figure 2a. It consists of 45 tissue types whose thermal and dielectric properties are taken from the IT'IS [27] database at $500\ MHz$.

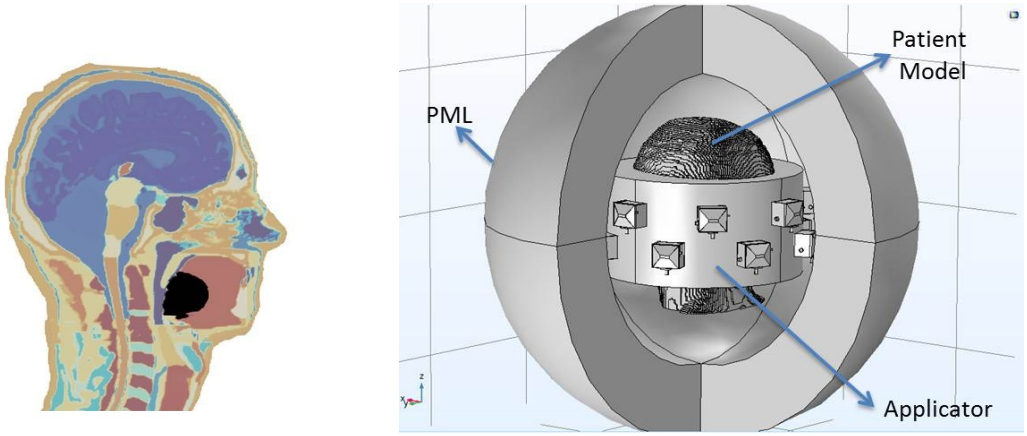

(a) (b)

Fig. 2. (**a**) Sagittal cut of the original voxel model with the tumor shown in black. (**b**) The overall simulation setup consisting of the applicator, the patient model, and the surrounding spherical PML in Comsol.

Unfortunately, Comsol at its current version does not offer any functionality of importing a voxel model, nor is there any easy-to-use CAD model of the patient that can be directly imported into the platform. As suggested by [28], there is, however, an ingenious workaround that allows the property mapping of sophisticated scenarios into the mask of the physical object (or patient in this case). In other words, instead of building the CAD model of each and every internal organ and putting them together (while trying to avoid self-intersecting faces and other complications of a sophisticated CAD model), we can use the powerful material interpolation function in Comsol in order to indirectly define the irregular and intricate internal tissues within the overall mask of the patient body. Following this procedure, the mask of the patient's head was imported into Comsol and the internal tissue properties were interpolated with $1\ mm$ resolution.

Among all types of antennas proposed for biomedical applications [29]–[32], the open ridged waveguide (ORWG) antenna [33] was selected in this study to build a 16-element circular phased array applicator. The proposed configuration has two rings of interlaced elements with an inter-ring distance of $5\ cm$. An in-between matching medium, which can be a water bolus or a hydrogel, was set to be $14\ cm$ in both diameter and height, as shown in Figure 2b. Detailed discussions on the optimal size and configuration of a one-size-fits-all applicator for the head and neck (H&N) region can be found in [11, 34].

B. Treatment planning procedure

In this study, we used the hybrid beamforming technique of time-reversal plus particle swarm optimization (TR+PSO) to maximize the specific absorption rate (SAR) on the tumor. SAR (W/Kg) is related to the power loss density (PLD) (W/m^3) through the mass density ρ of each tissue, i.e. $SAR = PLD/\rho$. A thorough discussion of the algorithm as well as the steps needed to be taken in its implementation have been given elsewhere [11, 22] and thus will not be repeated here. Suffice it to say that to avoid getting trapped in local minima, TR fast solution was used as an educated guess to initialize the PSO routine, thereby speeding up the whole optimization process.

C. Bioheat thermal simulation and the assessment of different FEM-based simulators

In the context of HT therapy, the deposited EM energy in terms of PLD eventually turns into heat due to the Joule heating effect. And the biological models involve perfused tissues because of the blood circulation in the patient body. Now, taking into account the blood perfusion rate, the simplest way to model this phenomenon is by using the Pennes Bioheat equation [35] as follows:

$$c_p \rho \frac{\partial T}{\partial t} = \nabla \cdot (k \nabla T) + PLD - c_b w_b (T - T_b) \tag{1}$$

where T $(^\circ C)$ is temperature; ρ (kg/m^3) is mass density; c_p $(J/^\circ C/kg)$ is heat capacity; k $(W/^\circ C/m)$ is thermal conductivity; and T_b, c_b, w_b $(kg/m^3/s)$ are temperature, heat capacity, and perfusion rate of blood, respectively.

While one can pick commercial solvers such as CST or Comsol as their package of choice to tackle such a multi-physics problem to some extent, we have observed technical issues and challenges with both software packages. For instance, CST uses only hexahedron meshes for thermal simulations of biological models. This limits the ability of its solver to conform the meshes to the natural curvature of the biological structures/ tissues and as a result, it can give rise to staircase temperature approximations at tissue borders, as earlier pointed out and discussed for E-field calculations and distributions as well.

Comsol, on the other hand, uses the tetrahedron mesh type which is more flexible for conformal meshing, but we experienced some issues working with Comsol too. First and foremost and as discussed already, due to the current inability of Comsol's geometric kernel to handle big models, we had to resort to the dielectric mapping workaround instead of importing the whole physical body model into the platform. This certainly introduces some approximations due to dielectric interpolation at tissue borders. Secondly, in its Bioheat kernel implementation, Comsol assigns one perfusion rate to the whole patient body, i.e. there is currently no means in Comsol to allow for a tissue-specific blood perfusion rate. This can compromise the accuracy of the resultant temperature distribution in a noticeable way because as proved in the biological studies, tumorous cells have a much lower perfusion rate than healthy tissues, something that actually works in favor of HT.

Considering all the above-mentioned shortcomings of the commercial packages, we believe that a modular, open-source computational engine provides more flexibility to model, simulate, and optimize the treatment planning workflow. It can also save a lot of computational time upon an efficient parallel implementation for heavy models. Therefore, to provide the means of thermal validation and cross-checking in this study, we also chose to, after exporting the EM field from Comsol, repeat the thermal simulation part with a powerful FEM-based computational engine called FEniCS [36]. Tetrahedron mesh generation for the FEniCS solver was done by Iso2mesh [37], an open-source Matlab/Octave-based package that allows for the tissue-specific assignment of blood perfusion rate and other thermal properties by giving each tissue type a unique identifier. Interested readers can consult [11] for thorough instructions on how to use FEniCS in Bioheat simulations. Plus, an excerpt of the Python code used for the FEniCS simulation in this study can be found in Appendix A.

D. Differential microwave thermometry method

The temperature dependence of dielectric properties of biological tissues ($\Delta\epsilon$, $\Delta\sigma$, or $\Delta O = |\Delta\epsilon_r + \frac{j}{\omega\epsilon_b}\Delta\sigma|$) makes it possible to detect the temperature changes during an HT treatment. The challenges in the hyperthermic mild increase above the normal body temperature ($[4-7]\ ^\circ C$) lie in (a) the detection of small changes in the tissue dielectric properties which are typically less than 1% per $^\circ C$ [38] and (b) in the proper conversion of $\Delta\epsilon$, $\Delta\sigma$, or ΔO into temperature. The magnitude of these dielectric changes in the microwave frequency range depends on the tissue water content. Dielectric spectroscopies on animal tissue [39] show that the high-water content tissue such as muscle and liver, for instance, exhibit larger changes in their dielectric properties during heating while the low-water content tissues such as fat and bone show significantly lower temperature dependencies.

The linear least-square method (LS) is used as the inversion technique in this study. It typically has a smooth kernel, meaning that the solution is highly sensitive to small perturbations in the data and is therefore ill-posed. A wide variety of regularization schemes to deal with the ill-posedness of inverse problems have been proposed in the literature among which Tikhonov [40] is one of the most popular and efficient methods. While all the derivations of LS formulas and Tikhonov regularization along with the detailed discussion of the time-stepped method are given elsewhere [14], we summarize the inversion procedure here in an easy-to-follow pseudo-code/ flowchart for only the last time step or steady-state thermometry.

Using the same notation as in [14], we can relate ΔO at each time step (t_s) to the differential S-parameter input pair of i and j, i.e. $\Delta S_{ji,sca} = S_{ji,sca}(t_s) - S^b_{ji,sca} = S_{ji,tot}(t_s) - S^b_{ji,tot}$ according to the following standard Fredholm integral equation of the first kind [12]

$$\Delta S^{sca}_{ji}(\omega) \simeq C \int_\Omega \mathbf{E}^{Comsol}_{inc,j}(\mathbf{r}',\omega)\cdot \Delta O(\mathbf{r}',\omega)\mathbf{E}^{Comsol}_{inc,j}(\mathbf{r}',\omega)dv'. \tag{2}$$

After discretizing the Region of Interest (RoI) and considering A as the discretized linear forward operator, equation (2) can be written as

$$Am = d \tag{3}$$

with $m = \Delta O$ and $d = \Delta S$ where m is the contrast function that relates to the dielectric changes due to temperature and hence is the sought-after unknown in this equation, and d is the differential input to the algorithm. This equation in the familiar linear algebraic form is ill-posed and hence requires a regularization scheme. To solve this problem, Tikhonov functional is defined as follows [41]

$$F(m) = \frac{1}{2}\|Am - d\|^2_{L_2} + \frac{\lambda}{2}\|m\|^2_{L_2} \tag{4}$$

where $\|.\|_{L_2}$ is an $L2$-norm operator while λ is the Tikhonov regularization parameter. Finally, the minimization of Equation 4 leads to the reconstruction of thermograms using the solution matrix m. Steps taken in the least-square reconstruction are summarized in Algorithm 1.

Algorithm 1 LS Reconstruction

1: **Base-line scenario at $t = 0$:** Extract both the electric field distribution of the RoI and S-matrix $[S^B]$ from Comsol.

2: **Steady-state S-matrix:** Measure the S-matrix $[S^{SS}]$ at the last temporal step of $[T_n]$

3: **The differential input to the algorithm:** For time step n, calculate the differential steady-state input $d^n = [S^B] - [S^{SS}]$ and feed it to the algorithm.

4: **Image reconstruction based on DBA method:** Having the linear forward operator A at hand, form the linear-algebraic equation of $Am^n = d^n$ to find the contrast function m^n at the last time step.

5: **Minimization of the Tikhonov functional:** Solve the above mentioned equation through minimization of the Tikhonov functional using the Singular Value Decomposition (SVD) method.

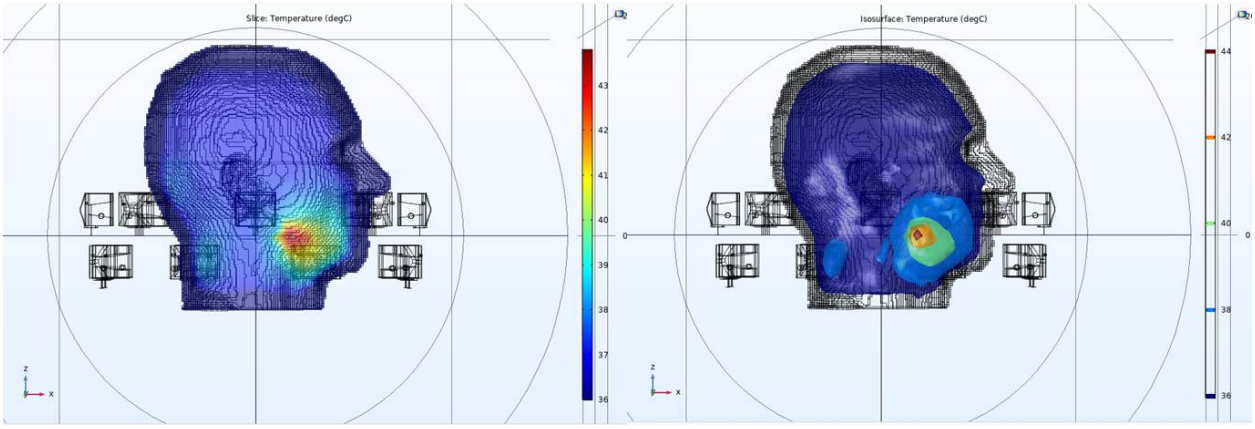

(a) Temperature distribution (b) Thermal Iso-contours

Fig. 3. Sagittal cut of the steady-state Comsol thermal simulation.

III. Results & Discussion

A. Comsol temperature distributions

After exporting all the E-field distributions produced by sequential ports excitation in Comsol, the hybrid beamforming of TR+PSO was applied in Matlab in order to find the optimal phased array setting for this specific scenario, i.e. the optimal amplitudes and phases of the 16 ports that would steer the focal point on the tumor. Combining the E-fields under the assumption that we excited all ports simultaneously with the optimal amplitudes and phases, we then obtained the steady-state thermal profiles reported in Figure 3. As can be seen, the method was successful in making a mild temperature gradient between the tumor and the surrounding healthy tissue of about $7°C$ above the normal body temperature (i.e. in the range of $[37 - 44]°C$). To better emphasize where the potential hotspots for this specific treatment planning may emerge, the thermal Iso-contour plot is also shown in Figure 3b which shows an undesirable area of relatively high temperature (up to $40°C$) at the back of the patient's neck.

B. Comparison between Comsol and FEniCS thermal results

The first row of subplots, in the transverse, coronal, and sagittal planes, respectively, of Figure 4 shows the thermal profiles coming from Comsol simulation while the second row shows those of FEniCS. To get a more quantitative measure of the comparison between the two sets, the profiles of the 2D cutlines passing through the center of the tumor in each plane have been also reported in the third row. Although there is a good agreement between the two solvers, the FEniCS profiles are smoother than those of Comsol. This was expected because thanks to the parallel implementation in FEniCS, we had no limitations on the mesh density and/or on the node numbers while Comsol could only handle the scenario up to $100K$ mesh nodes before it started to crash. Therefore, higher mesh density of FEniCS (around 250K mesh nodes) was partly responsible for smoother final results. As mentioned in subsection II-C, the inability of Comsol versus FEniCS in assigning tissue-specific perfusion rates can be another contributing factor to the differences in the two sets of thermal profiles.

C. Thermograms of the change in constitutive parameters due to thermal stress

As a result of the beamformed HT administration, the thermal stress in the steady-state case was from normal body temperature ($37°C$) up to $44°C$ in the tumor center. Using the thermal distribution pattern produced by FEniCS in subsection III-B and assuming a 1% dielectric change per $°C$ according to in-vivo measurements in animal liver tissue [38], this mild range of about $7°C$ was assumed to make up to 7% dielectric change in the modified Comsol setup which was then used to obtain $[S^{SS}]$. Subsequently, $[S^{SS}]$ was fed into the differential input of the inversion algorithm.

The result of the reconstruction method is shown in Figure 5. As can be seen, there are some strong variations, especially at the air-skin boundary of the reconstructed model. However, due to the cooling effect of the surface water bolus that enforces a fixed Dirichlet boundary condition of $20°C$ throughout the thermal simulation, these sharp indicators cannot account for the emergence of real hot spots but are rather reconstruction artifacts. Advanced mesh refinement/ image restoration techniques, such as the adaptive finite element method (AFEM) [14, 15], can be used in future studies to improve the reconstruction quality by suppressing these spurious indicators. Other than that and as can be seen from the Iso-contours of Figure 5b, the reconstruction was successful in retrieving the location of the focal point on the tumor where in reality the dielectric changes are at their maximum.

Last but not least, the reconstructed profiles are qualitative indicators of the dielectric changes, normalized between zero and one. To provide clinicians with more interpretable results in the process of clinical integration of this technique, there needs to be a mapping technique developed to translate these unitless normalized indicators to the real temperature evolution in $°C$ during the course of HT treatment. This also remains to be investigated in future studies.

IV. Conclusion

Even after several decades of active research, the use of microwave technologies in cancer therapies, aka microwave HT, still faces several clinical challenges among which is the need for a real-time heat monitoring feedback mechanism. While the invasive, painful thermometry method of fiber optic probes is still practiced in the

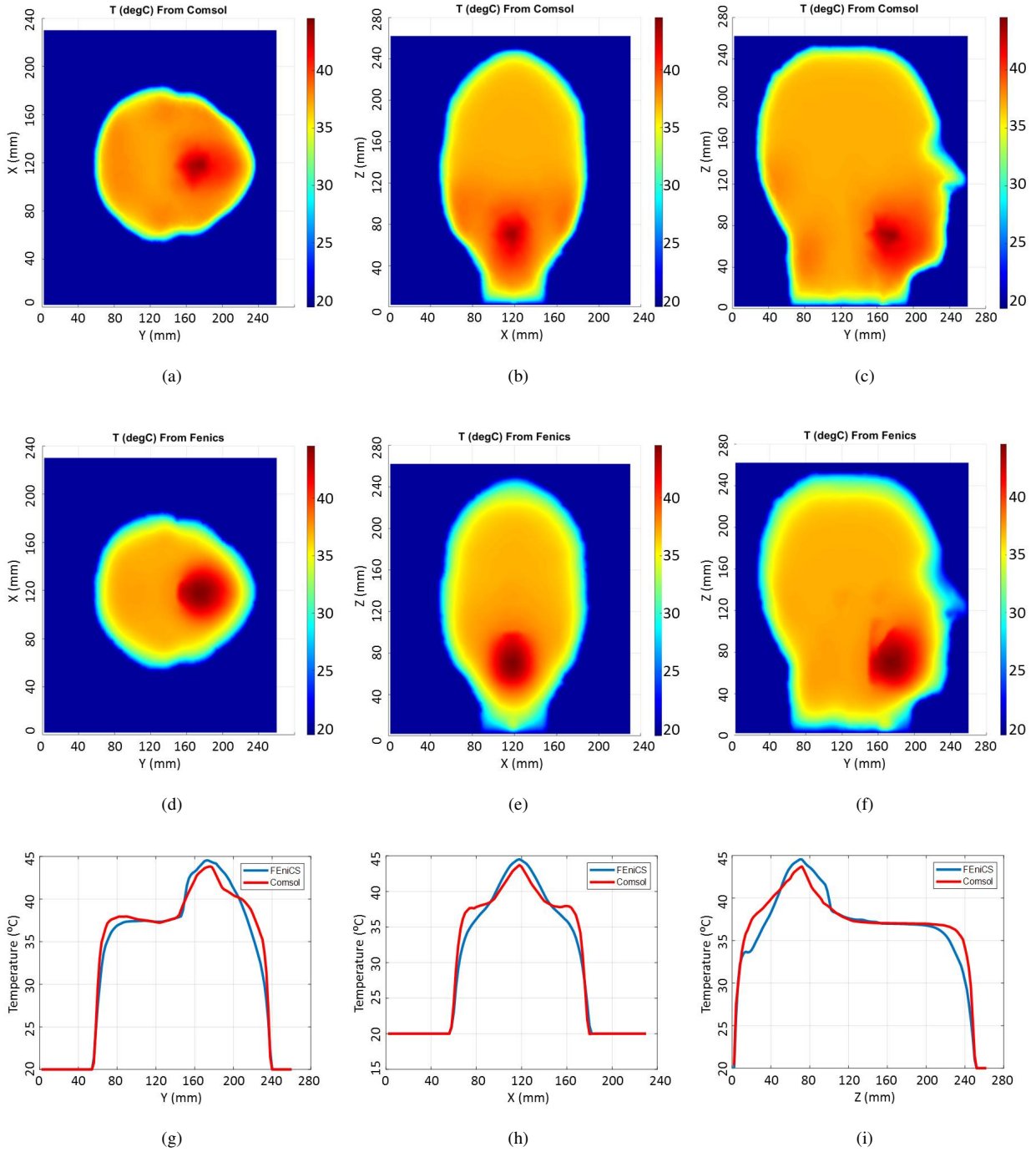

Fig. 4. Reported in the first, second, and third columns are the steady-state temperature distributions in transverse, coronal, and sagittal planes, respectively. The first row(**a**, **b**, and **c**) represents the thermal results of Comsol. The second row (**d**, **e**, and **f**) shows the thermal result of the same model produced by FEniCS. The third row (**g**, **h**, and **i**) compares the two sets of results from Comsol and FEniCS along the 2D cutlines passing through the center of the tumor in each plane.

field, there has been a growing demand and trend toward non-invasive, safer methods. Microwave thermometry is a non-invasive potential candidate to provide reliable thermal feedback for HT systems while at the same time

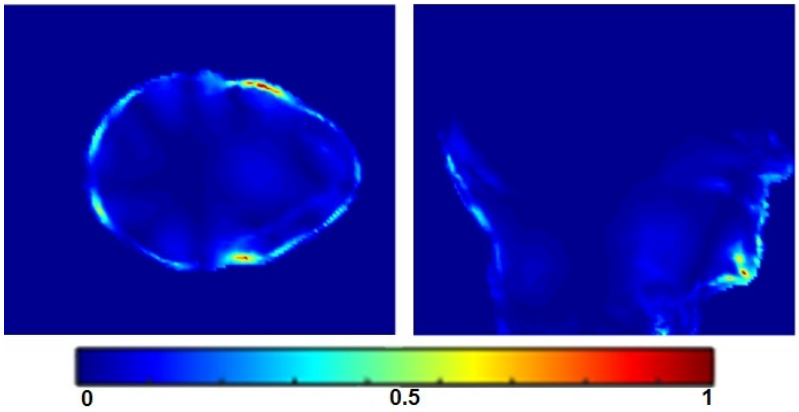

(a) Thermograms

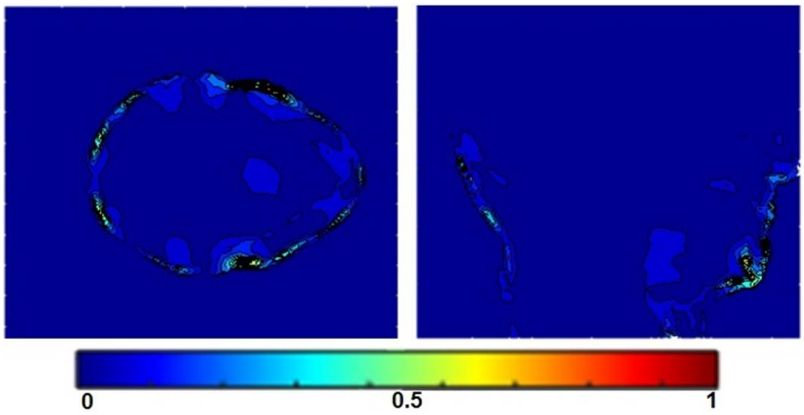

(b) Iso-contours at level 0.3 of the reconstructed thermograms

Fig. 5. Reconstructed thermograms, in the transverse and sagittal planes, respectively, that show qualitative changes in the constitutive parameters of the region under treatment.

offering a compact and cost-effective solution. While dealing with the challenges that inversion algorithms may encounter in a realistic scenario, this feasibility study also shows the suitability of the method. When it comes to the quality of the final thermograms, there is, of course, room for improvement that can be investigated in future studies by applying an adaptive FEM mesh refinement scheme or other image restoration techniques. Given the limited ranges in which Hyperthermic temperatures change, the sensitivity of the thermometry method needs to be very high so as to detect small variations of constitutive parameters under relatively mild thermal stress. This might be less of an issue in ablation therapies where the range of temperature change is at least an order of magnitude higher than HT, albeit under those acute and intense heating regimes, the deformation of the region under treatment necessitates a reconfigurable dynamic meshing scheme to track the thermal evolution in a real-time manner.

APPENDIX A

AN EXCERPT OF THE PYTHON CODE USED FOR BIOHEAT SIMULATION IN FENICS

```
from fenics import *
import scipy.io as sio
import numpy as np

Tb = Constant(37)   #Arterial blood temperature
Bolus_Temp = Constant(20)
Body_Temp = Constant(37) #Normal body temperature

#%% Modern Mesh conversion
mesh = Mesh()
with XDMFFile(mesh.mpi_comm(),"SIO/GeoDukeTongue.xdmf") as infile:
    infile.read(mesh)

mvc = MeshValueCollection("size_t",mesh,3)
with XDMFFile(mesh.mpi_comm(),"SIO/cf.xdmf") as infile:
    infile.read(mvc, "name_to_read")
Markers = cpp.mesh.MeshFunctionSizet(mesh,mvc)

mvc = MeshValueCollection("size_t",mesh,2)
with XDMFFile(mesh.mpi_comm(),"SIO/mf.xdmf") as infile:
    infile.read(mvc, "name_to_read")
BCs = cpp.mesh.MeshFunctionSizet(mesh,mvc)

dx = Measure("dx", domain=mesh, subdomain_data=Markers)

#%% Boundary Condition and initial value
V = FunctionSpace(mesh, 'CG', 1)
Outer_bc = DirichletBC(V, Bolus_Temp, DomainBoundary())

#%% Subdomains' property assignment
V0 = FunctionSpace(mesh, 'DG', 0)
Kapa = Function(V0)
Cp = Function(V0)
WbCb = Function(V0)
Rho = Function(V0)

#read the subdomain XDMF file stored by the serial part for this process.
with XDMFFile(mesh.mpi_comm(),'SIO/Kapa.xdmf') as file:
    file.read_checkpoint(Kapa,'K',0)

with XDMFFile(mesh.mpi_comm(),'SIO/Cp.xdmf') as file:
    file.read_checkpoint(Cp,'C',0)

with XDMFFile(mesh.mpi_comm(),'SIO/WbCb.xdmf') as file:
    file.read_checkpoint(WbCb,'W',0)

with XDMFFile(mesh.mpi_comm(),'SIO/Rho.xdmf') as file:
    file.read_checkpoint(Rho,'R',0)

#%% Impressed Source Definition from PLD on FEM nodes!
FTermSpace = FunctionSpace(mesh, 'CG', 1)  # so that dofs are only in mesh vertices
f = Function(FTermSpace)

#read the source back from XDMF file stored by the serial part.
with XDMFFile(mesh.mpi_comm(),'SIO/Q.xdmf') as file:
```

```
    file.read_checkpoint(f,'Source',0)

#%% Define Variational Problem
T = TrialFunction(V)
w = TestFunction(V)

#%% Symbolic Steady-State Bioheat equation
F = Kapa*dot(grad(T), grad(w))*dx + WbCb*(T - Tb)*w*dx - f*w*dx
a, L = lhs(F), rhs(F)

# Compute the solution
T = Function(V)
solve(a == L, T, Outer_bc)

#%% Exporting the Result
with XDMFFile('DukeVisulization/TemperatureHO.xdmf') as xdmf:
    xdmf.write_checkpoint(T,'T0c',0)

vtkfile = File('DukeVisulization/Temperature.pvd')
vtkfile << T

print('Completed!')
```

REFERENCES

[1] D. L. Colton, R. Kress, and R. Kress, *Inverse acoustic and electromagnetic scattering theory*. Springer, 1998, vol. 93.

[2] X. Chen, *Computational methods for electromagnetic inverse scattering*. John Wiley & Sons, 2018.

[3] M. Pastorino, *Microwave imaging*. John Wiley & Sons, 2010, vol. 208.

[4] M. Ghaderi Aram, M. Haghparast, M. Abrishamian, and A. Mirtaheri, "Comparison of imaging quality between linear sampling method and time reversal in microwave imaging problems," *Inverse Problems in Science and Engineering*, vol. 24, no. 8, pp. 1347–1363, 2016.

[5] M. F. Imani, J. N. Gollub, O. Yurduseven, A. V. Diebold, M. Boyarsky, T. Fromenteze, L. Pulido-Mancera, T. Sleasman, and D. R. Smith, "Review of metasurface antennas for computational microwave imaging," *IEEE transactions on antennas and propagation*, vol. 68, no. 3, pp. 1860–1875, 2020.

[6] R. Zoughi, *Microwave non-destructive testing and evaluation principles*. Springer Science & Business Media, 2000, vol. 4.

[7] R. Persico, *Introduction to ground penetrating radar: inverse scattering and data processing*. John Wiley & Sons, 2014.

[8] M. Ghaderi Aram, M. Dehmollaian, and A. Khaleghi, "Buried target imaging: A comparative study," *Sensing and Imaging*, vol. 18, pp. 1–19, 2017.

[9] N. K. Nikolova, "Microwave imaging for breast cancer," *IEEE microwave magazine*, vol. 12, no. 7, pp. 78–94, 2011.

[10] J. W. Hand, K. Hynynen, P. Shrivastava, and T. Saylor, *Methods of external hyperthermic heating*. Springer Science & Business Media, 2012.

[11] M. G. Aram, *Antenna Design, Radiobiological Modelling, and Non-Invasive Monitoring for Microwave Hyperthermia*. Chalmers Tekniska Hogskola (Sweden), 2022.

[12] M. Haynes, J. Stang, and M. Moghaddam, "Real-time microwave imaging of differential temperature for thermal therapy monitoring," *IEEE Transactions on Biomedical Engineering*, vol. 61, no. 6, pp. 1787–1797, 2014.

[13] G. Chen, J. Stang, M. Haynes, E. Leuthardt, and M. Moghaddam, "Real-time three-dimensional microwave monitoring of interstitial thermal therapy," *IEEE Transactions on Biomedical Engineering*, vol. 65, no. 3, pp. 528–538, 2017.

[14] M. G. Aram, L. Beilina, and H. D. Trefna, "Microwave thermometry with potential application in non-invasive monitoring of hyperthermia," *Journal of Inverse and Ill-posed Problems*, vol. 28, no. 5, pp. 739–750, 2020.

[15] L. Beilina, M. G. Aram, and E. M. Karchevskii, "An adaptive finite element method for solving 3d electromagnetic volume integral equation with applications in microwave thermometry," *Journal of Computational Physics*, vol. 459, p. 111122, 2022.

[16] M. M. Paulides, P. R. Stauffer, E. Neufeld, P. F. Maccarini, A. Kyriakou, R. A. Canters, C. J. Diederich, J. F. Bakker, and G. C. Van Rhoon, "Simulation techniques in hyperthermia treatment planning," *International Journal of Hyperthermia*, vol. 29, no. 4, pp. 346–357, 2013.

[17] E. Schena, D. Tosi, P. Saccomandi, E. Lewis, and T. Kim, "Fiber optic sensors for temperature monitoring during thermal treatments: an overview," *Sensors*, vol. 16, no. 7, p. 1144, 2016.

[18] P. Wust, C. H. Cho, B. Hildebrandt, and J. Gellermann, "Thermal monitoring: invasive, minimal-invasive and non-invasive approaches," *International Journal of Hyperthermia*, vol. 22, no. 3, pp. 255–262, 2006.

[19] L. Winter, E. Oberacker, K. Paul, Y. Ji, C. Oezerdem, P. Ghadjar, A. Thieme, V. Budach, P. Wust, and T. Niendorf, "Magnetic resonance thermometry: Methodology, pitfalls and practical solutions," *International Journal of Hyperthermia*, vol. 32, no. 1, pp. 63–75, 2016.

[20] F. Adibzadeh, K. Sumser, S. Curto, D. T. Yeo, A. A. Shishegar, and M. M. Paulides, "Systematic review of pre-clinical and clinical devices for magnetic resonance-guided radiofrequency hyperthermia," *International Journal of Hyperthermia*, vol. 37, no. 1, pp. 15–27, 2020.

[21] R. M. Arthur, W. Straube, J. Trobaugh, and E. Moros, "Non-invasive estimation of hyperthermia temperatures with ultrasound," *International journal of hyperthermia*, vol. 21, no. 6, pp. 589–600, 2005.

[22] M. G. Aram, H. Aliakbarian, and H. D. Trefná, "A phased array applicator based on open ridged-waveguide antenna for microwave hyperthermia," *Microwave and Optical Technology Letters*, vol. 63, no. 12, pp. 3086–3091, 2021.

[23] M. Ghaderi Aram, M. Zanoli, H. Nordström, I. Toma-Dasu, K. Blomgren, and H. Dobšíček Trefná, "Radiobiological evaluation of combined gamma knife radiosurgery and hyperthermia for pediatric neuro-oncology," *Cancers*, vol. 13, no. 13, p. 3277, 2021.

[24] M. Haynes and M. Moghaddam, "Vector green's function for s-parameter measurements of the electromagnetic volume integral equation," *IEEE transactions on antennas and propagation*, vol. 60, no. 3, pp. 1400–1413, 2011.

[25] M. Haynes, J. Stang, and M. Moghaddam, "Microwave breast imaging system prototype with integrated numerical characterization," *Journal of Biomedical Imaging*, vol. 2012, pp. 2–2, 2012.

[26] A. Christ, W. Kainz, E. G. Hahn, K. Honegger, M. Zefferer, E. Neufeld, W. Rascher, R. Janka, W. Bautz, J. Chen *et al.*, "The virtual family—development of surface-based anatomical models of two adults and two children for dosimetric simulations," *Physics in Medicine & Biology*, vol. 55, no. 2, p. N23, 2009.

[27] P. Hasgall, F. Di Gennaro, C. Baumgartner, E. Neufeld, B. Lloyd, M. Gosselin, D. Payne, A. Klingenböck, and N. Kuster, "It'is database for thermal and electromagnetic parameters of biological tissues," *Version 4.0*, 2018.

[28] H. Gothäll, "How to use interpolated material data to model irregular geometries," *Comsol Blog*, 2018.

[29] M. M. Paulides, J. F. Bakker, N. Chavannes, and G. C. Van Rhoon, "A patch antenna design for application in a phased-array head and neck hyperthermia applicator," *IEEE Transactions on Biomedical Engineering*, vol. 54, no. 11, pp. 2057–2063, 2007.

[30] R. K. Amineh, A. Trehan, and N. K. Nikolova, "Tem horn antenna for ultra-wide band microwave breast imaging," *Progress In Electromagnetics Research B*, vol. 13, pp. 59–74, 2009.

[31] J. Yang and A. Kishk, "A novel low-profile compact directional ultra-wideband antenna: the self-grounded bow-tie antenna," *IEEE Transactions on Antennas and Propagation*, vol. 60, no. 3, pp. 1214–1220, 2011.

[32] S. M. Aguilar, M. A. Al-Joumayly, M. J. Burfeindt, N. Behdad, and S. C. Hagness, "Multiband miniaturized patch antennas for a compact, shielded microwave breast imaging array," *IEEE transactions on antennas and propagation*, vol. 62, no. 3, pp. 1221–1231, 2013.

[33] M. Ghaderi Aram, H. Aliakbarian, and H. Dobšíček Trefná, "An ultra-wideband compact design for hyperthermia: Open ridged-waveguide antenna," *IET Microwaves, Antennas & Propagation*, vol. 16, no. 2-3, pp. 137–152, 2022.

[34] E. Oberacker, A. Kuehne, C. Oezerdem, J. Nadobny, M. Weihrauch, M. Beck, S. Zschaeck, C. Diesch, T. W. Eigentler, H. Waiczies *et al.*, "Radiofrequency applicator concepts for thermal magnetic resonance of brain tumors at 297 mhz (7.0 tesla)," *International Journal of Hyperthermia*, vol. 37, no. 1, pp. 549–563, 2020.

[35] E. H. Wissler, "Pennes' 1948 paper revisited," *Journal of applied physiology*, vol. 85, no. 1, pp. 35–41, 1998.

[36] M. Alnæs, J. Blechta, J. Hake, A. Johansson, B. Kehlet, A. Logg, C. Richardson, J. Ring, M. E. Rognes, and G. N. Wells, "The fenics project version 1.5," *Archive of Numerical Software*, vol. 3, no. 100, 2015.

[37] Q. Fang and D. A. Boas, "Tetrahedral mesh generation from volumetric binary and grayscale images," in *2009 IEEE international symposium on biomedical imaging: from nano to macro*. Ieee, 2009, pp. 1142–1145.

[38] M. Lazebnik, M. C. Converse, J. H. Booske, and S. C. Hagness, "Ultrawideband temperature-dependent dielectric properties of animal liver tissue in the microwave frequency range," *Physics in Medicine & Biology*, vol. 51, no. 7, p. 1941, 2006.

[39] S. Ley, S. Schilling, O. Fiser, J. Vrba, J. Sachs, and M. Helbig, "Ultra-wideband temperature dependent dielectric spectroscopy of porcine tissue and blood in the microwave frequency range," *Sensors*, vol. 19, no. 7, p. 1707, 2019.

[40] C. R. Vogel, *Computational methods for inverse problems*. SIAM, 2002.

[41] A. N. Tikhonov, A. Goncharsky, V. Stepanov, and A. G. Yagola, *Numerical methods for the solution of ill-posed problems*. Springer Science & Business Media, 2013, vol. 328.